A two-dimensional vertical non-hydrostatic σ model with an implicit method for free-surface flows

Hengliang Yuan and Chin H. Wu[*,†]

Department of Civil and Environmental Engineering, 1269D Engineering Hall, University of Wisconsin, Madison, WI 53706-1691, U.S.A.

SUMMARY

An implicit finite difference model in the σ co-ordinate system is developed for non-hydrostatic, two-dimensional vertical plane free-surface flows. To accurately simulate interaction of free-surface flows with uneven bottoms, the unsteady Navier–Stokes equations and the free-surface boundary condition are solved simultaneously in a regular transformed σ domain using a fully implicit method in two steps. First, the vertical velocity and pressure are expressed as functions of horizontal velocity. Second, substituting these relationship into the horizontal momentum equation provides a block tri-diagonal matrix system with the unknown of horizontal velocity, which can be solved by a direct matrix solver without iteration. A new treatment of non-hydrostatic pressure condition at the top-layer cell is developed and found to be important for resolving the phase of wave propagation. Additional terms introduced by the σ co-ordinate transformation are discretized appropriately in order to obtain accurate and stable numerical results. The developed model has been validated by several tests involving free-surface flows with strong vertical accelerations and non-linear waves interacting with uneven bottoms. Comparisons among numerical results, analytical solutions and experimental data show the capability of the model to simulate free-surface flow problems. Copyright © 2004 John Wiley & Sons, Ltd.

KEY WORDS: implicit; σ co-ordinate; non-hydrostatic pressure; free-surface flows

1. INTRODUCTION

Numerical modelling for simulating free-surface flows using the incompressible Navier–Stokes equations (NSE) has been intensively investigated in recent years [1–4]. In most of these models, it is assumed that the vertical acceleration is small so that a hydrostatic assumption can be used. This assumption is generally valid for simulating flows where the horizontal scale of motion is much larger than the vertical motion. However, for applications involving

---

*Correspondence to: Chin H. Wu, Department of Civil and Environmental Engineering, 1269D Engineering Hall, University of Wisconsin, Madison, WI 53706-1691, U.S.A.
†E-mail: chinwu@engr.wisc.edu

conditions such as short period waves, abruptly changing bed topographies, and stratification due to strong density gradients, the hydrostatic assumption is no longer valid. The use of the non-hydrostatic pressure distribution, resulting in solving the complete NSE, is necessary [5–8].

For simulating free-surface evolution with the complete NSE the well-known methods are the Marker-and-Cell (MAC) method [9] and the volume of fluid (VOF) method [10]. Another technique for tracking the free surface is the arbitrary Lagrangian–Eulerian (ALE) method [11], which is based on surface adaptive grids with a moving frame of references. All MAC, VOF and ALE methods have been used to simulate complicated free-surface flows such as breaking waves [12–14]. However, these methods require high computational expense and are limited by severe stability restriction [15, 16]. Issues of applying these models to large-scale geophysical and environmental flow problems remain [17].

In recent years, efforts have been devoted to develop cost-effective free-surface flow models based upon the non-hydrostatic pressure distribution. For example, a semi-implicit fractional step method [18] offers the advantage of efficiency and stability by solving the NSE in two steps. For the first step the derivative of the surface elevation in the hydrostatic momentum equation and the velocity in the continuity equation are discretized implicitly but the convective and horizontal viscosity terms are discretized explicitly. For the second step the non-hydrostatic pressure component is obtained by requiring the estimated velocity field in the first step to be convergent, resulting in solving the pressure Poisson equation (PPE). The flow field components are then corrected by adding the calculated non-hydrostatic pressure. Other efficient models are based on an explicit projection method [16, 19, 20], in which the NSE is advanced in time to obtain projected velocities by solving advection and diffusion terms explicitly. The projected velocities are then corrected by solving the PPE. While the progress for simulating unsteady free-surface flow using the semi-implicit fractional step method and the explicit projection method is ongoing, the cost of solving the PPE remains an issue for many practical applications [20]. Recently a fully implicit method with the only unknown of horizontal velocity was successfully developed by Namin *et al.* [21] to simulate non-hydrostatic free-surface flows by solving a block tri-diagonal matrix. Compared to the PPE systems, the block tri-diagonal system implicitly incorporates the vertical velocity and pressure into the horizontal momentum equation. Therefore, the NSE and free-surface boundary conditions can be solved simultaneously, without any intermediate value being introduced. In addition, while both the block tri-diagonal system and PPE system share the same matrix dimensions, iterative methods (e.g. the conjugate gradient method) are usually used to solve PPE of a sparse matrix system (e.g. five diagonal system for Cartesian two-dimensional vertical plane problem). In contrast, a direct matrix solver (e.g. double-sweep method and cyclic reduction method) can readily work for the block tri-diagonal system without any iteration.

The terrain-following σ co-ordinate is widely used for modelling free-surface flows over irregular bottoms [1, 5, 14, 16, 20]. Being one type of boundary-fitted co-ordinates, the σ co-ordinate is capable to vertically transform the varying topography into a regular domain. Boundary conditions at both the free surface and the bottom can thus be accurately represented. Therefore, the σ co-ordinate is widely applied in both the hydrostatic models [1] and the non-hydrostatic models. For example, two-dimensional and three-dimensional σ non-hydrostatic models with the semi-implicit fractional step method were developed by Stansby and Zhou [14] and Kocyigit *et al.* [22]. The explicit projection method was also incorporated to the σ non-hydrostatic model for water wave simulations [16, 19]. To date, the

numerical scheme for the fully implicit method was only in the Cartesian co-ordinate [21]. Implementation of fully implicit method in σ co-ordinate is yet developed.

In this paper, the implicit method for solving the complete NSE is extended to the σ co-ordinate. Maintaining the advantage of the boundary-fitted co-ordinate, the developed model can simultaneously solve all flow field components within each time step. The features make the model capable for simulating free-surface flows over irregular geometries. Without employing hydrostatic pressure representation at the centre of free-surface layer, a non-hydrostatic pressure expression for free-surface cells is derived. In the following sections, mathematical formulations and boundary conditions in both the Cartesian and the σ co-ordinates are given first. Numerical method is presented next. Finally, model results are compared to analytical solutions and/or experimental data for several examples: standing wave oscillation in a closed basin, solitary wave propagation in constant and variable water depths, and periodic wave propagation over a submerged bar.

2. MATHEMATICAL FORMULATION

2.1. Governing equations and boundary conditions in the Cartesian co-ordinate

For incompressible flows in the two-dimensional vertical plane, the Navier–Stokes equations in the Cartesian co-ordinate (x^*, z^*, t^*) are

$$\frac{\partial u}{\partial x^*} + \frac{\partial w}{\partial z^*} = 0 \tag{1}$$

$$\frac{\partial u}{\partial t^*} + u\frac{\partial u}{\partial x^*} + w\frac{\partial u}{\partial z^*} = -\frac{\partial P}{\partial x^*} + v\left(\frac{\partial^2 u}{\partial x^{*2}} + \frac{\partial^2 u}{\partial z^{*2}}\right) \tag{2}$$

$$\frac{\partial w}{\partial t^*} + u\frac{\partial w}{\partial x^*} + w\frac{\partial w}{\partial z^*} = -\frac{\partial P}{\partial z^*} + v\left(\frac{\partial^2 w}{\partial x^{*2}} + \frac{\partial^2 w}{\partial z^{*2}}\right) - g \tag{3}$$

where u and w are velocity components in the x^*- and z^*-direction, respectively; t^* is time; P is the normalized pressure, defined as the pressure divided by the density; g is the gravitational acceleration; and v is the kinematic viscosity.

Various surface boundary conditions are needed for solving Equations (1)–(3). The kinematic boundary condition at the impermeable bottom is

$$u\frac{\partial h}{\partial x^*} + w = 0 \tag{4}$$

where $h(x^*)$ is the water depth measured from the undisturbed mean water level (Figure 1(a)). Similarly, the kinematic boundary condition at the free surface is

$$\frac{\partial \eta}{\partial t^*} + u\frac{\partial \eta}{\partial x^*} = w \tag{5}$$

where $\eta(x^*, t^*)$ is the free-surface elevation measured from the undisturbed mean water level. The conservative form of free-surface equation can be obtained by integrating continuity
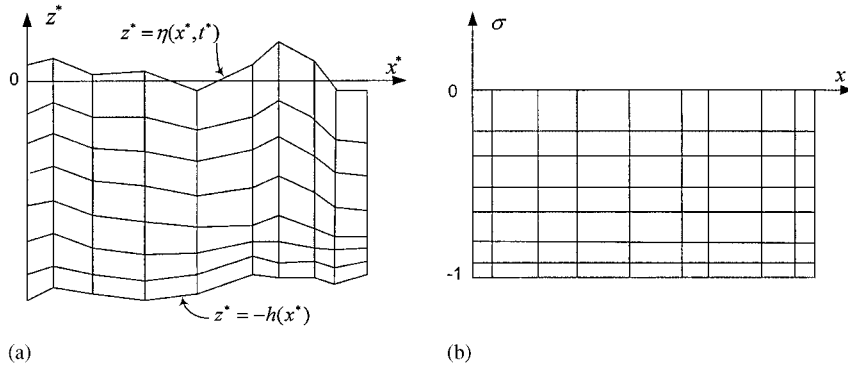
Figure 1. The σ co-ordinate transformation between (a) real physical and (b)
transformed computational mesh.

equation (1) over depth and applying the kinematic boundary conditions (4) and (5),
giving

$$\frac{\partial \eta}{\partial t^*} + \frac{\partial}{\partial x^*} \int_{-h}^{\eta} u \, \mathrm{d}z^* = 0 \tag{6}$$

The wind induced shear stress at the free surface is

$$\rho v \frac{\partial u}{\partial z^*} = (\tau_{tn})_{\mathrm{air}} \tag{7}$$

where $(\tau_{tn})_{\mathrm{air}}$ denotes the wind stress in the x^*-direction. The continuity of normal stress
$(\tau_{nn})_{\mathrm{air}}$ across the free surface is assumed. In the case of no wind, both shear stress $(\tau_{tn})_{\mathrm{air}}$
and $(\tau_{nn})_{\mathrm{air}}$ are then set to be zero. In addition, the pressure at the free surface is equal to
atmospheric pressure, taken as zero, i.e.

$$P_{z^* = \eta} = 0 \tag{8}$$

The inflow and outflow boundary conditions are also needed for simulating free-surface
wave propagation. At the inflow boundary, the velocity is given. At the outflow, a radiation
boundary condition is applied, i.e.

$$\frac{\partial \phi}{\partial t^*} + c \frac{\partial \phi}{\partial x^*} = 0 \tag{9}$$

where c is the wave celerity, and ϕ can be η, u or w.

2.2. Governing equations and boundary conditions in the σ co-ordinate

To simulate flows over irregular geometries, a terrain-following σ co-ordinate enables the
bottom boundary and the free surface to be better resolved [23]. Following Reference [24],
the transformation between the σ co-ordinate and the Cartesian co-ordinate is given as

$$t = t^*, \quad x = x^*, \quad \sigma = \frac{z^* - \eta}{h + \eta} = \frac{z^* - \eta(x,t)}{H(x,t)} \tag{10}$$

where H is the total water depth. The transformation maps a time-dependent physical, real domain into a stationary uniform transformed σ domain, resulting in $\sigma = -1$ at the bottom and $\sigma = 0$ at the free surface (Figure 1(b)).

Based upon the principle of chain differentiation, the governing equations (1)–(3) in the new co-ordinate (x, σ, t) are

$$\frac{\partial u}{\partial x} + \frac{\partial u}{\partial \sigma} \frac{\partial \sigma}{\partial x^*} + \frac{1}{H} \frac{\partial w}{\partial \sigma} = 0 \tag{11}$$

$$\frac{\partial u}{\partial t} + u \frac{\partial u}{\partial x} + w_\sigma \frac{\partial u}{\partial \sigma} = -\left(\frac{\partial P}{\partial x} + \frac{\partial P}{\partial \sigma} \frac{\partial \sigma}{\partial x^*} \right) + v \nabla_\sigma^2 u \tag{12}$$

$$\frac{\partial w}{\partial t} + u \frac{\partial w}{\partial x} + w_\sigma \frac{\partial w}{\partial \sigma} = -\frac{\partial P}{\partial \sigma} \frac{\partial \sigma}{\partial z^*} + v \nabla_\sigma^2 w - g \tag{13}$$

where

$$\frac{\partial \sigma}{\partial x^*} = -\frac{1}{H} \left(\frac{\partial \eta}{\partial x^*} + \sigma \frac{\partial H}{\partial x^*} \right) \tag{14a}$$

$$\nabla_\sigma^2 = \frac{\partial^2}{\partial x^2} + 2 \left(\frac{\partial \sigma}{\partial x^*} \right) \frac{\partial^2}{\partial x \partial \sigma} + \left[\left(\frac{\partial \sigma}{\partial x^*} \right)^2 + \left(\frac{\partial \sigma}{\partial z^*} \right)^2 \right] \frac{\partial^2}{\partial \sigma^2} \tag{14b}$$

$$\frac{\partial \sigma}{\partial z^*} = \frac{1}{H} \tag{14c}$$

and

$$w_\sigma = \frac{D\sigma}{Dt^*} = -\frac{1}{H} (1 + \sigma) \frac{\partial \eta}{\partial t^*} - \frac{u}{H} \left(\frac{\partial \eta}{\partial x^*} + \sigma \frac{\partial H}{\partial x^*} \right) + \frac{w}{H} \tag{14d}$$

It should be noted that, in the case of flows over a steep topography, the σ co-ordinate transformation could introduce numerical errors in calculating the horizontal pressure gradient and the horizontal diffusion [25, 26]. Special numerical treatments to address this problem have been well documented [27]. In this paper, we do not include the treatment since our applications only involve free-surface flows over topographies with mild steepness. Thus, the numerical results are free of the steepness-introduced errors.

For the boundary conditions in the σ co-ordinate, the Dirichlet-type condition remains the same as the Cartesian form, i.e.

$$P_{\sigma=0} = 0 \tag{15}$$

However, the Neumann-type condition, i.e. any derivative of velocity, free surface or pressure, needs to be transformed. Using Equation (10), boundary conditions (4), (6) and (9) are

expressed in the σ co-ordinate as

$$u \frac{\partial h}{\partial x} + w_\sigma = 0 \tag{16}$$

$$\frac{\partial \eta}{\partial t} + \frac{\partial}{\partial x} \left(H \int_{-1}^{0} u \, \mathrm{d}\sigma \right) = 0 \tag{17}$$

$$\frac{\partial \phi}{\partial t} + \frac{\partial \phi}{\partial \sigma} \frac{\partial \sigma}{\partial t^*} + c \left(\frac{\partial \phi}{\partial x} + \frac{\partial \phi}{\partial \sigma} \frac{\partial \sigma}{\partial x^*} \right) = 0 \tag{18}$$

3. NUMERICAL METHOD

In this paper, a finite difference approximation is used to discretize the governing equations and boundary conditions in the σ co-ordinate. A staggered grid mesh system with a set of uniform rectangular $M \times N$ cells in x- and σ-direction is employed. The velocity components are defined at the sides for each cell, and the pressure and free-surface elevation are located at the centre of the cell (Figure 2).

A fully implicit scheme with a central difference in space is used in two steps. First, the vertical velocity and pressure are expressed as functions of horizontal velocities. Second, substituting these relationship into the horizontal momentum equation gives a block tri-diagonal matrix system with unknown horizontal velocities, which can be directly solved. The overall accuracy of the scheme is second-order in space and second-order in time under a 0.5 implicit time weighting factor. Details of the implicit method in the Cartesian co-ordinate can be referred to Reference [21]. In this paper, we extend the implicit method to the σ co-ordinate. Special attention is paid to the treatment of non-hydrostatic pressure condition at the top-layer cell. Additional terms introduced by the σ co-ordinate transformation are also discretized appropriately in order to obtain accurate and stable numerical results. Details of the numerical method are given below.

Continuity equation: The continuity equation (11) is discretized implicitly at the point (i,k) as

$$\frac{u_{i+1/2,k}^{n+1} - u_{i-1/2,k}^{n+1}}{\Delta x} + \frac{u_{i+1/2,k+1}^{n+1} + u_{i-1/2,k+1}^{n+1} - u_{i+1/2,k-1}^{n+1} - u_{i-1/2,k-1}^{n+1}}{4\Delta\sigma} \left(\frac{\partial\sigma}{\partial x^*} \right)_{i,k}^{n}$$

$$+ \frac{1}{H_i^n} \frac{w_{i,k+1/2}^{n+1} - w_{i,k-1/2}^{n+1}}{\Delta\sigma} \approx 0 \tag{19}$$

where the term $(\partial\sigma/\partial x^*)_{i,k}^{n}$ is discretized as

$$\left(\frac{\partial\sigma}{\partial x^*} \right)_{i,k}^{n} \approx -\frac{1}{H_i^n} \left(\frac{\eta_{i+1/2}^n - \eta_{i-1/2}^n}{\Delta x} + \sigma_k \frac{H_{i+1/2}^n - H_{i-1/2}^n}{\Delta x} \right) \tag{20}$$

The above discretization is sequentially applied from the bottom cell, $k = 1$, to the free-surface cell, $k = N$, (Figure 2). Being expressed as the function of the adjacent horizontal velocities,
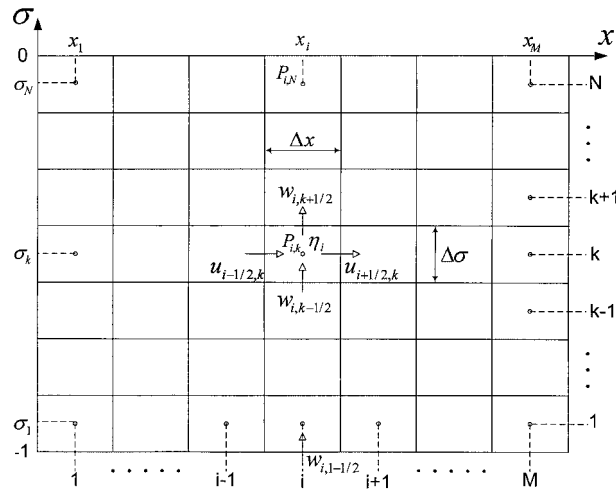
Figure 2. The staggered grid mesh in the σ co-ordinate.

the vertical velocity at each layer (i.e. $k = 1, 2, \ldots, N$) is

$$w_{i,k+1/2}^{n+1} \approx w_{i,1-1/2}^{n+1} - \frac{H_i^n \Delta \sigma}{\Delta x} \sum_{j=1}^{k} (u_{i+1/2,j}^{n+1} - u_{i-1/2,j}^{n+1})$$

$$- \frac{H_i^n}{4} \sum_{j=1}^{k} \left[(u_{i+1/2,j+1}^{n+1} + u_{i-1/2,j+1}^{n+1} - u_{i+1/2,j-1}^{n+1} - u_{i-1/2,j-1}^{n+1}) \left(\frac{\partial \sigma}{\partial x^*} \right)_{i,k}^{n} \right] \qquad (21)$$

where $w_{i,1-1/2}^{n+1}$ is the known vertical velocity from the bottom boundary condition.

Vertical momentum equation: To represent the pressure at each layer below except for the top one (i.e. $k = 1, 2, \ldots, N - 1$) by the horizontal velocity, the vertical momentum equation (13) is used. The discretization of each term in the equation at the point $(i, k + 1/2)$ is given below:

$$\frac{\partial w}{\partial t} \approx \frac{w_{i,k+1/2}^{n+1} - w_{i,k+1/2}^{n}}{\Delta t} \qquad (22)$$

$$u \frac{\partial w}{\partial x} \approx u_{i,k+1/2}^{n+1} \frac{w_{i+1,k+1/2}^{n} - w_{i-1,k+1/2}^{n}}{2\Delta x} \qquad (23)$$

$$w_\sigma \frac{\partial w}{\partial \sigma} \approx (w_\sigma)_{i,k+1/2}^{n} \frac{w_{i,k+3/2}^{n+1} - w_{i,k-1/2}^{n+1}}{2\Delta \sigma} \qquad (24)$$

$$\frac{\partial P}{\partial \sigma} \frac{\partial \sigma}{\partial z^*} = \frac{1}{H} \frac{\partial P}{\partial \sigma} \approx \frac{1}{H_i^n} \left[\theta_{vm} \left(\frac{P_{i,k+1}^{n+1} - P_{i,k}^{n+1}}{\Delta \sigma} \right) + (1 - \theta_{vm}) \left(\frac{P_{i,k+1}^{n} - P_{i,k}^{n}}{\Delta \sigma} \right) \right] \qquad (25)$$

where θ_{vm} is the implicit weighting factor, $0 < \theta_{vm} < 1$, and

$$
\nabla_\sigma^2 w \approx \left(\frac{\partial^2 w}{\partial x^2} \right)_{i,k+1/2}^n + 2 \left(\frac{\partial \sigma}{\partial x^*} \right)_{i,k+1/2}^n \left(\frac{\partial^2 w}{\partial x \partial \sigma} \right)_{i,k+1}^n
$$

$$
+ \left[\left(\frac{\partial \sigma}{\partial x^*} \right)^2 + \left(\frac{\partial \sigma}{\partial z^*} \right)^2 \right]_{i,k+1/2}^n \left(\frac{\partial^2 w}{\partial \sigma^2} \right)_{i,k+1/2}^n \tag{26}
$$

where the discretized form of $(\partial \sigma / \partial x^*)$ can be referred to Equation (20), the calculation of $(\partial \sigma / \partial z^*)$ are shown in Equation (14c), and

$$
\left(\frac{\partial^2 w}{\partial x^2} \right)_{i,k+1/2}^n \approx \frac{(\partial w / \partial x)_{i+1/2,k+1/2}^n - (\partial w / \partial x)_{i-1/2,k+1/2}^n}{\Delta x} \tag{27a}
$$

$$
\left(\frac{\partial^2 w}{\partial x \partial \sigma} \right)_{i,k+1/2}^n \approx \frac{(\partial w / \partial \sigma)_{i+1/2,k+1/2}^n - (\partial w / \partial \sigma)_{i-1/2,k+1/2}^n}{\Delta x} \tag{27b}
$$

$$
\left(\frac{\partial^2 w}{\partial \sigma^2} \right)_{i,k+1/2}^n \approx \frac{(\partial w / \partial \sigma)_{i,k+1}^n - (\partial w / \partial \sigma)_{i,k}^n}{\Delta \sigma} \tag{27c}
$$

By substituting Equations (22)–(27) into Equation (13), the pressure at the lower layer can be written as function of the upper-layer pressure and the velocities, i.e.

$$
P_{i,k}^{n+1} \approx P_{i,k+1}^{n+1} + a_{k0} w_{i,k-1/2}^{n+1} + a_{k1} w_{i,k+1/2}^{n+1} + a_{k2} w_{i,k+3/2}^{n+1}
$$

$$
+ a_{k3} u_{i-1/2,k}^{n+1} + a_{k4} u_{i-1/2,k+1}^{n+1} + a_{k5} u_{i+1/2,k}^{n+1} + a_{k6} u_{i+1/2,k+1}^{n+1} + a_{k7} \tag{28}
$$

where

$$
a_{k0} = \frac{H_i^n \Delta \sigma}{\theta_{vm}} \left(-\frac{(w_\sigma)_{i,k+1/2}^n}{2 \Delta \sigma} - \frac{v}{(H_i^n \Delta \sigma)^2} \right)
$$

$$
a_{k1} = \frac{H_i^n \Delta \sigma}{\theta_{vm}} \left(\frac{1}{\Delta t} + \frac{2v}{(H_i^n \Delta \sigma)^2} \right)
$$

$$
a_{k2} = \frac{H_i^n \Delta \sigma}{\theta_{vm}} \left(\frac{(w_\sigma)_{i,k+1/2}^n}{2 \Delta \sigma} - \frac{v}{(H_i^n \Delta \sigma)^2} \right)
$$

$$
a_{k3} = \frac{H_i^n \Delta \sigma}{\theta_{vm}} \left(\frac{w_{i+1,k+1/2}^n - w_{i-1,k+1/2}^n}{8 \Delta x} \right)
$$

$$
a_{k4} = a_{k5} = a_{k6} = a_{k3}
$$

$$a_{k7} = \frac{H_i^n \Delta\sigma}{\theta_{vm}} \left\{ -\frac{1}{\Delta t} w_{i,k+1/2}^n + (1 - \theta_{vm}) \frac{P_{i,k+1}^n - P_{i,k}^n}{\Delta\sigma} \right.$$

$$\left. -g - v\left[\frac{\partial}{\partial x^*}\left(\frac{\partial w}{\partial x^*}\right)\right]_{i,k+1/2}^n - v\left[\frac{\partial}{\partial \sigma}\left(\frac{\partial w}{\partial x^*}\right)\frac{\partial \sigma}{\partial x^*}\right]_{i,k+1/2}^n \right\}$$

Equation (28) is valid from the bottom layer, $k = 1$, to the one below the top layer, $k = N - 1$. Further treatment of the pressure at the top layer, $k = N$, is necessary.

Pressure at the free-surface cell: In the staggered grid system, the top-layer pressure is generally treated by employing the hydrostatic approximation [20–22]. Difficulties of representing the top-layer pressure in the non-hydrostatic flow exist [17, 18]. In this paper, both hydrostatic and non-hydrostatic components are included in the top-layer pressure, i.e.

$$P_{\sigma=\sigma_N} = \frac{g(h+\eta)\Delta\sigma}{2} + \frac{\partial}{\partial t}\int_{\sigma_N}^0 (Hw)\,\mathrm{d}\sigma + \frac{\partial}{\partial x}\int_{\sigma_N}^0 (Huw)\,\mathrm{d}\sigma - (Hw_\sigma w)\bigg|_{\sigma=\sigma_N} \tag{29}$$

where σ_N represents the centre of the top-layer cells (see Figure 2) and $H = h + \eta$. Equation (29) is analytically derived by integrating the vertical momentum equation (13) over half of the top-layer cell and applying $w_\sigma = 0$ at the free surface. The advantage of applying Equation (29) is to algebraically represent the top-layer pressure by the free-surface elevation (the first term in the right-hand side) and the vertical acceleration (the rest of the terms in the right-hand side).

A linearization approximation is used to discretize Equation (29), giving

$$P_{i,N}^{n+1} = \frac{g\Delta\sigma H_i^{n+1}}{2} + \frac{\Delta\sigma w_{i,N}^n}{2}\frac{H_i^{n+1} - H_i^n}{\Delta t} + \frac{\Delta\sigma H_i^n}{2}\frac{w_{i,N}^{n+1} - w_{i,N}^n}{\Delta t}$$

$$+ \frac{\Delta\sigma(uw)_{i,N}^n}{2}\frac{H_{i+1/2}^n - H_{i-1/2}^n}{\Delta x} + \frac{\Delta\sigma(Hw)_{i,N}^n}{2}\frac{u_{i+1/2,N}^{n+1} - u_{i-1/2,N}^{n+1}}{\Delta x}$$

$$+ \frac{\Delta\sigma(Hu)_{i,N}^n}{2}\frac{w_{i+1/2,N}^n - w_{i-1/2,N}^n}{\Delta x}$$

$$- \frac{(w_\sigma w)_{i,N}^n H_i^{n+1} + (w_\sigma H)_{i,N}^n w_{i,N}^{n+1} + (wH)_{i,N}^n w_\sigma^n}{3} \tag{30}$$

where $H_i^{n+1} = h_i + \eta_i^{n+1}$, $w_{i,N}^{n+1} = (w_{i,N-1/2}^{n+1} + w_{i,N+1/2}^{n+1})/2$, and $w_{i,N}^n = (w_{i,N-1/2}^n + w_{i,N+1/2}^n)/2$. To further express the top-layer pressure by horizontal velocity, the free-surface equation (17) is discretized and rearranged as

$$\eta_i^{n+1} \approx \eta_i^n - \theta_{fs}\frac{\Delta t\Delta\sigma}{\Delta x}\left(H_{i+1/2}^n\sum_{k=1}^N u_{i+1/2,k}^{n+1} - H_{i-1/2}^n\sum_{k=1}^N u_{i-1/2,k}^{n+1}\right)$$

$$- (1 - \theta_{fs})\frac{\Delta t\Delta\sigma}{\Delta x}\left(H_{i+1/2}^n\sum_{k=1}^N u_{i+1/2,k}^n - H_{i-1/2}^n\sum_{k=1}^N u_{i-1/2,k}^n\right) \tag{31}$$

where θ_{fs} is the implicit weighting factor with $0 < \theta_{fs} < 1$. Substituting Equation (31) into Equation (30) yields the top-layer pressure

$$P_{i,N}^{n+1} = a_{N0} w_{i,N-1/2}^{n+1} + a_{N1} w_{i,N+1/2}^{n+1} + a_{N2} u_{i-1/2,N}^{n+1} + a_{N3} u_{i+1/2,N}^{n+1}$$

$$+ a_{N4} \sum_{k=1}^{N} u_{i-1/2,k}^{n+1} + a_{N5} \sum_{k=1}^{N} u_{i+1/2,k}^{n+1} + a_{N6} \tag{32}$$

where

$$a_{N0} = \frac{\Delta\sigma H_i^n}{2\Delta t} - \frac{(w_\sigma H)_{i,N}^n}{3}$$

$$a_{N1} = a_{N0}$$

$$a_{N2} = -\frac{\Delta\sigma(Hw)_{i,N}^n}{2\Delta x}$$

$$a_{N3} = -a_{N2}$$

$$a_{N4} = \left[\frac{g\Delta\sigma}{2} + \frac{\Delta\sigma w_{i,N}^n}{2\Delta t} - \frac{(w_\sigma w)_{i,N}^n}{3} \right] \left(\theta_{fs} H_{i-1/2}^n \frac{\Delta t \Delta\sigma}{\Delta x} \right)$$

$$a_{N5} = \left[\frac{g\Delta\sigma}{2} + \frac{\Delta\sigma w_{i,N}^n}{2\Delta t} - \frac{(w_\sigma w)_{i,N}^n}{3} \right] \left(-\theta_{fs} H_{i+1/2}^n \frac{\Delta t \Delta\sigma}{\Delta x} \right)$$

$$a_{N6} = -\frac{\Delta\sigma w_{i,N}^n H_i^n}{\Delta t} + \frac{\Delta\sigma(uw)_{i,N}^n}{2} \frac{H_{i+1/2}^n - H_{i-1/2}^n}{\Delta x} + \frac{\Delta\sigma(Hu)_{i,N}^n}{2} \frac{w_{i+1/2,N}^n - w_{i-1/2,N}^n}{\Delta x}$$

$$- \frac{(w_\sigma w H)_{i,N}^n}{3} + \left[\frac{g\Delta\sigma}{2} + \frac{\Delta\sigma w_{i,N}^n}{2\Delta t} - \frac{(w_\sigma w)_{i,N}^n}{3} \right]$$

$$\times \left[H_i^n - (1 - \theta_{fs}) \frac{\Delta t \Delta\sigma}{\Delta x} \left(H_{i+1/2}^n \sum_{k=1}^{N} u_{i+1/2,k}^n - H_{i-1/2}^n \sum_{k=1}^{N} u_{i-1/2,k}^n \right) \right]$$

In both Equations (32) for the top layer and Equation (28) for layers below the top layer, the pressure is an implicit function of horizontal and vertical velocities. The vertical velocity is further eliminated by substituting Equation (21) into Equations (32) and (28), giving a matrix form

$$\bar{P}_i^{n+1} = \bar{\bar{B}}_i \bar{U}_{i-1/2}^{n+1} + \bar{\bar{C}}_i \bar{U}_{i+1/2}^{n+1} + \bar{D}_i \tag{33}$$

where the double overbar denotes a two-dimensional matrix and the single overbar denotes a vector. The pressure at each layer thus can be written as the function of the adjacent horizontal velocities with coefficients in the matrices $\bar{\bar{B}}_i$, $\bar{\bar{C}}_i$ and $\bar{D}_i$ which can be determined from Equations (28) and (32).

Horizontal momentum equation: The second step of the implicit method is to obtain a block tri-diagonal matrix system with the only unknown of horizontal velocity by eliminating the vertical velocity and pressure from the horizontal momentum equation (12). The discretization

of each term in Equation (12) at the point $(i+1/2,k)$ from the bottom layer, $k=1$, to the top layer, $k=N$, is given below:

$$\frac{\partial u}{\partial t} \approx \frac{u_{i+1/2,k}^{n+1} - u_{i+1/2,k}^{n}}{\Delta t} \qquad (34)$$

$$u\,\frac{\partial u}{\partial x} \approx u_{i+1/2,k}^{n}\,\frac{u_{i+3/2,k}^{n+1} - u_{i-1/2,k}^{n+1}}{2\Delta x} \qquad (35)$$

$$w_\sigma\,\frac{\partial u}{\partial \sigma} \approx (w_\sigma)_{i+1/2,k}^{n}\,\frac{u_{i+1/2,k+1}^{n+1} - u_{i+1/2,k-1}^{n+1}}{2\Delta \sigma} \qquad (36)$$

$$\left(\frac{\partial P}{\partial x} + \frac{\partial P}{\partial \sigma}\frac{\partial \sigma}{\partial x^*}\right) \approx \theta_{hm}\left[\frac{P_{i+1,k}^{n+1} - P_{i,k}^{n+1}}{\Delta x} + \frac{P_{i,k+1}^{n+1} + P_{i+1,k+1}^{n+1} - P_{i,k-1}^{n+1} - P_{i+1,k-1}^{n+1}}{4\Delta\sigma}\left(\frac{\partial \sigma}{\partial x^*}\right)_{i+1/2,k}^{n}\right]$$

$$+ (1-\theta_{hm})\left[\frac{P_{i+1,k}^{n} - P_{i,k}^{n}}{\Delta x}\right.$$

$$\left. + \frac{P_{i,k+1}^{n} + P_{i+1,k+1}^{n} - P_{i,k-1}^{n} - P_{i+1,k-1}^{n}}{4\Delta\sigma}\left(\frac{\partial \sigma}{\partial x^*}\right)_{i+1/2,k}^{n}\right] \qquad (37)$$

where θ_{hm} is the implicit weighting factor with $0<\theta_{hm}<1$, and

$$\nabla_\sigma^2 u \approx \left(\frac{\partial^2 u}{\partial x^2}\right)_{i+1/2,k}^{n} + 2\left(\frac{\partial \sigma}{\partial x^*}\right)_{i+1/2,k}^{n}\left(\frac{\partial^2 u}{\partial x\partial\sigma}\right)_{i+1/2,k}^{n}$$

$$+ \left[\left(\frac{\partial \sigma}{\partial x^*}\right)^2 + \left(\frac{\partial \sigma}{\partial z^*}\right)^2\right]_{i+1/2,k}^{n}\left(\frac{\partial^2 u}{\partial \sigma^2}\right)_{i+1/2,k}^{n} \qquad (38)$$

where $(\partial^2 u/\partial x^2)_{i+1/2,k}^{n}$, $(\partial^2 u/\partial x\partial\sigma)_{i+1/2,k}^{n}$ and $(\partial^2 u/\partial \sigma^2)_{i+1/2,k}^{n}$ share the same discretization scheme as Equation (27). Substituting Equations (34)–(38) into Equation (12) yields a matrix form with the horizontal velocity and pressure as

$$\bar{\bar{E}}_1 \bar{U}_{i-1/2}^{n+1} + \bar{\bar{F}}_1 \bar{P}_{i}^{n+1} + \bar{\bar{E}}_2 \bar{U}_{i+1/2}^{n+1} + \bar{\bar{F}}_2 \bar{P}_{i+1}^{n+1} + \bar{\bar{E}}_3 \bar{U}_{i+3/2}^{n+1} = \bar{G}_0 \qquad (39)$$

where the coefficient matrices can be obtained from Equations (34)–(38).

Eliminating the pressure in Equation (39) by using Equation (33) yields

$$\bar{\bar{E}}_l \bar{U}_{i-1/2}^{n+1} + \bar{\bar{E}}_m \bar{U}_{i+1/2}^{n+1} + \bar{\bar{E}}_r \bar{U}_{i+3/2}^{n+1} = \bar{G}_1 \qquad (40)$$

where

$$\bar{\bar{E}}_l = \bar{\bar{E}}_1 + \bar{\bar{F}}_1 \bar{\bar{B}}_i$$

$$\bar{\bar{E}}_m = \bar{\bar{E}}_2 + \bar{\bar{F}}_1 \bar{\bar{C}}_i + \bar{\bar{F}}_2 \bar{\bar{B}}_{i+1}$$

$$\bar{\bar{E}}_r = \bar{\bar{E}}_3 + \bar{\bar{F}}_2 \bar{\bar{C}}_{i+1}$$

$$\bar{G}_1 = \bar{G}_0 - \bar{\bar{F}}_1 \bar{D}_i - \bar{\bar{F}}_2 \bar{D}_{i+1}$$

Equation (40) is a block tri-diagonal system with a dimension of $MN \times MN$, in which each block sub-matrix has a dimension of $N \times N$. The only unknown, $\bar{U}^{n+1}$, can be directly solved using the double-sweep method [28] with the appropriate boundary conditions. Once the horizontal velocity, u^{n+1} solved, w^{n+1}, η^{n+1} and P^{n+1} can be directly determined from Equations (21), (31) and (33), respectively, then w_σ^{n+1} can be updated from the discretized form of Equation (14d)

$$(w_\sigma)_{i,k+1/2}^{n+1} \approx - \frac{1 + \sigma_{k+1/2}}{H_i^{n+1}} \frac{\eta_i^{n+1} - \eta_i^n}{\Delta t}$$

$$- \frac{u_{i,k+1/2}^{n+1}}{H_i^{n+1}} \left(\frac{\eta_{i+1/2}^{n+1} - \eta_{i-1/2}^{n+1}}{\Delta x} + \sigma_{k+1/2} \frac{H_{i+1/2}^{n+1} - H_{i-1/2}^{n+1}}{\Delta x} \right) + \frac{w_{i,k+1/2}^{n+1}}{H_i^{n+1}} \qquad (41)$$

Radiation boundary condition: The radiation boundary condition (18) is discretized as

$$\frac{(\phi_{IB}^{n+1} + \phi_{IB-1}^{n+1}) - (\phi_{IB}^n + \phi_{IB-1}^n)}{2\Delta t} + \left(\frac{\partial \phi}{\partial \sigma} \right)_{IB}^n \left(\frac{\partial \sigma}{\partial t^*} \right)_{IB}^n$$

$$+ c \left[\frac{(\phi_{IB}^{n+1} + \phi_{IB}^n) - (\phi_{IB-1}^{n+1} + \phi_{IB-1}^n)}{2\Delta x} + \left(\frac{\partial \phi}{\partial \sigma} \right)_{IB}^n \left(\frac{\partial \sigma}{\partial x^*} \right)_{IB}^n \right] = 0 \qquad (42)$$

where $IB = M$ for $\phi = u$, and $IB = M + 1/2$ for $\phi = w$ or P. The upwind difference in space is used.

4. MODEL VALIDATIONS

Four examples of free-surface flow problems with significant non-hydrostatic pressure are chosen to evaluate the developed σ model. The third and fourth examples also test the capability of the model to simulate free-surface flows interacting with uneven bottoms.

The implicit weighting factors θ_{fs}, θ_{vm} and θ_{hm} in Section 3 are used in the numerical discretization for the free-surface equation (31), vertical momentum equation (25) and horizontal momentum equation (37), respectively. Similar implicit weighting factors have been suggested in other models [14, 18, 21, 22]. For the implicit method in the Cartesian co-ordinate, the factor values close to 0.5 were suggested to model short waves and higher values were needed to give more stable results for long-wave or steady-flow simulations [21]. For the present σ model, numerical tests show that the model is unconditionally stable by setting $\theta_{fs} \geqslant 0.5$, $\theta_{vm} \geqslant 0.5$ and $\theta_{hm} \geqslant 0.5$. In addition, the values around 0.9 for implicit weighting factors give the relative good results for both short-wave and long-wave simulations, suggesting the results are not sensitive to the implicit parameters. In following tests, $\theta_{fs} = \theta_{vm} = \theta_{hm} = 0.9$ are used without further adjustment.

4.1. Standing wave oscillation in a closed basin

A uninodal standing wave with an inviscid fluid in a closed basin is a good example for demonstrating the effects of hydrodynamic pressure distribution on model results. The length of the basin is $L = 10$ m and the equilibrium water depth is $h = 10$ m. The wave amplitude, $A = 0.1$, 1% of the water depth, is used here. The linear wave theory is valid in the case since the wave steepness, $2\pi A/2L = 0.031$. The analytical solution for linear wave period is $T = 3.588$ s and wave celerity is $c = 5.575$ m/s. Details of analytical solutions of the linear standing wave in the basin can be found in Reference [29].

In the model, the computational domain is discretized by a set of uniform $M \times N = 20 \times 20$ cells. A time step of $\Delta t = 0.05$ s is used. An initial free-surface elevation, $\eta = A \cos(2\pi x/2L)$, is prescribed and a zero initial velocity is assumed. At bottom the impermeability or free-slip (e.g. $\partial u/\partial \sigma = 0$) boundary conditions are applied. Comparisons of velocity and hydrodynamic pressure fields between the numerical results and analytical solutions at $t = T/8$, $T/2$ and $5T/8$ are given in Figure 3. While the velocity field between $x = 0$ and 5 m is downward at $t = T/8$, the velocity field between $x = 0$ and 5 m is upward at $t = 5T/8$. At $t = T/2$ the dynamic pressure reaches to the maximum value, corresponding to a null velocity fields. Generally, it can be seen that the numerical results are in excellent agreement with the analytical solutions based upon the linear wave theory. In Figure 4, time series for the free-surface elevation at $x = 0.25$ and 9.75 m using a hydrostatic approximation and the non-hydrostatic top-layer treatment are shown. Apparent phase error is observed using the hydrostatic representation at the top-layer cell. In contrast, both the wave amplitude and phase from the numerical predictions using the fully non-hydrostatic pressure at the top cell are well compared with the analytical solutions for the duration of 10 wave periods, suggesting that the implicit model is capable of simulating hydrodynamic pressure and velocity. Figure 5 shows the time series of horizontal velocity on the middle elevation of the water depth at $x = 2.25$ m. The numerical results with and without top-layer non-hydrostatic pressure treatment are also compared to the analytical solution. Phase error is clearly observed using the hydrostatic representation at the top-layer cell. The results from the fully non-hydrostatic model are in excellent agreement with the analytical solutions, indicating the importance of using the non-hydrostatic pressure at the free-surface cell.

To further address the accuracy and stability of the model, different time steps, $\Delta t = 0.0001$, 0.001, 0.01, 0.05, 0.1 and 0.2 s are used. Numerical results of the free-surface elevation, η_j, at $x = 0.25$ and 9.75 m are compared with the analytical solutions, $\tilde{\eta}_j$. The error between the numerical results and analytical solutions is measured by a norm

$$L_{\text{CYC}} = \sqrt{\frac{1}{N_{\text{CYC}}} \sum_{j=1}^{N_{\text{CYC}}} (\eta_j - \tilde{\eta}_j)^2}$$

where time cycles $N_{\text{CYC}} = T/\Delta t$, and $10T/\Delta t$, respectively. The numerical error from the present model using the different Courant numbers is shown in Table I. At $Cr = 0.558$ the model can predict the same accurate results for the free-surface elevation as those from the smaller Cr. For larger Courant numbers (e.g. $Cr = 1.115$), the prediction of the free-surface elevation is still promising, indicating the advantage of the model to simulate free-surface flows with less restricted time steps in comparison to the explicit numerical schemes.

Finally, mesh convergence test is performed to examine the sensitivity of the model on mesh resolution. Under a fixed Courant number, $Cr = 0.558$, four sets of mesh resolution (i.e.

10×10, 20×10, 20×20 and 40×20, described in the form of x-resolution $\times \sigma$-resolution)
are chosen here. The accuracy of numerical results is 20 evaluated by the norm, L_{CYC}, and the
comparisons are shown in Table II. The difference between the results using a mesh system
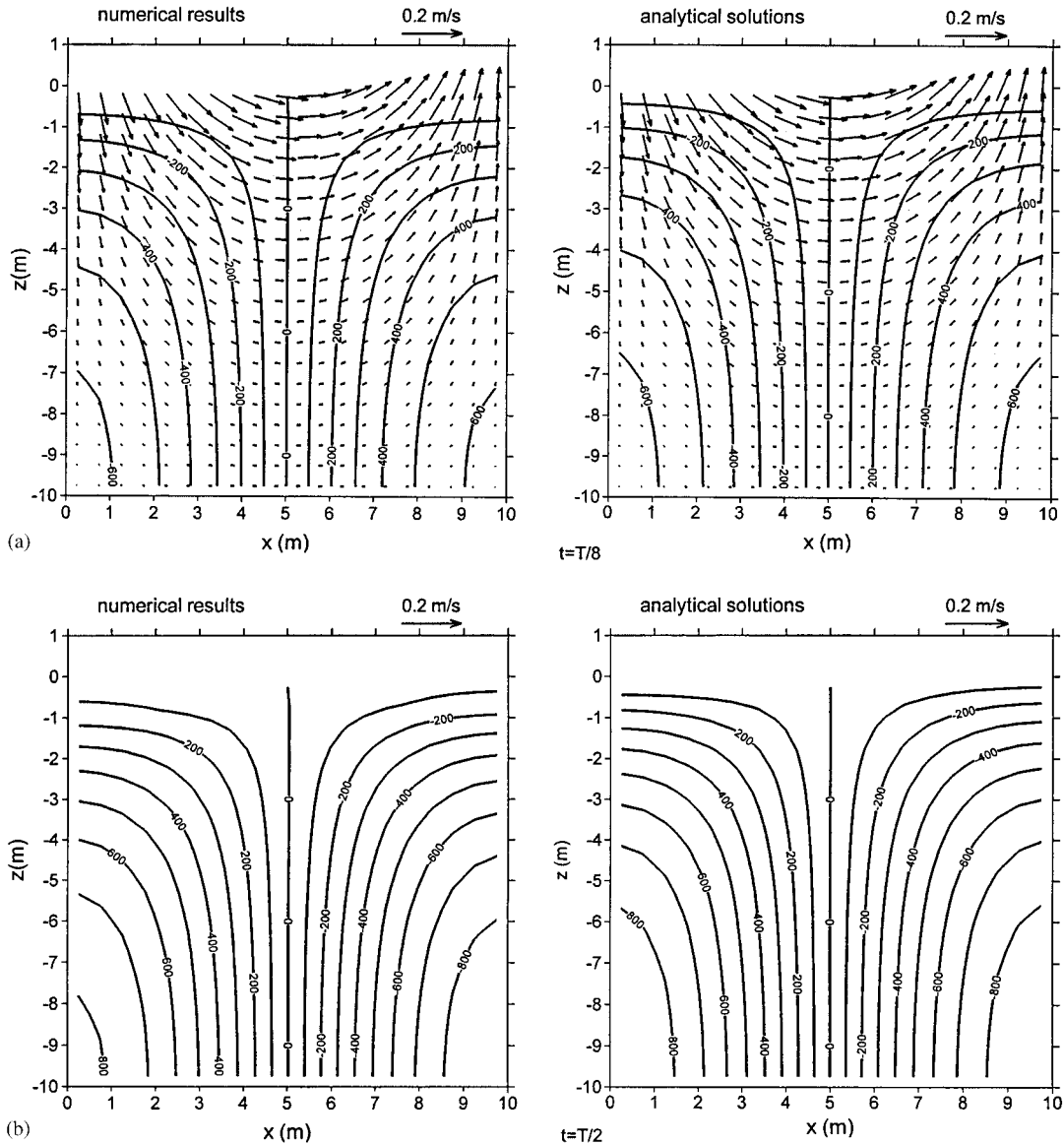of 20×20 and 40×20 is very small, indicating that the solution is convergent using a 20×20

Figure 3. Comparisons of velocity and dynamic pressure fields for standing wave oscillation in a closed
basin between numerical results and analytical solutions at (a) $t = \frac{1}{8}T$, (b) $t = \frac{1}{2}T$ and (c) $t = \frac{5}{8}T$. The
interval of each iso-line of dynamic pressure is 100 Pa.
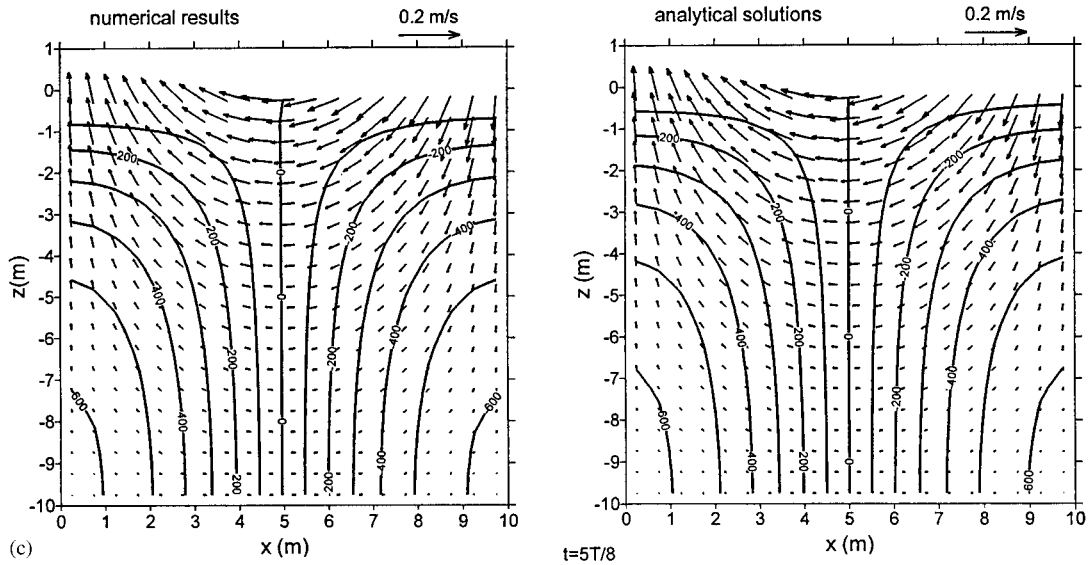
Figure 3. *Continued.*

mesh system. Moreover, Table II shows that a vertical resolution of 20 layers in this case is necessary for accurately simulating the free-surface elevation.

4.2. Solitary wave propagation in a constant water depth

The purpose of this test is to validate the model capability for simulating solitary wave propagation in a constant water depth. From the potential flow theory, a small amplitude solitary wave can propagate at a constant speed without changing its form and amplitude over a horizontal bottom [30].

To test the model, the viscosity is set to zero. A solitary wave with an amplitude of $A = 1.0$ m in a constant water depth $h = 10.0$ m is considered. The computational domain with the length of $L = 2000$ m is discretized by a set of uniform $M \times N = 1000 \times 10$ cells. Using a time step of $\Delta t = 0.1$ s, the Courant number is $Cr = c\Delta t / \Delta x = 0.519$ in this test, where the theoretical wave celerity $c = \sqrt{g(h + A)} = 10.388$ m/s. At left inflow boundary time series of the free-surface elevation and velocity based upon the analytical solution [31] are specified. The radiation boundary condition is imposed at the outflow boundary. The initial position of wave crest is specified at $x = -150$ m (out of the computational domain), enabling a null initial condition for both the free-surface elevation and velocities in the computational domain.

Figure 6 shows the comparisons of the free-surface elevation between the numerical results and analytical solutions at $t = 45$, 90, 135 and 180 s. The numerical results for both the wave profile and wave celerity are in excellent agreement with analytical solutions. The mass and energy are still well conserved after the wave has propagated about a distance of $200h$. Comparisons of horizontal and vertical velocities at the middle of the water elevation between the numerical results and analytical solutions at these times are shown in Figure 7. Some slightly noticeable difference occurs in the maximum horizontal velocity and vertical velocity.

Generally, numerical results are almost identical to the analytical solution, suggesting that the hydrodynamic pressure is accurately estimated by the model.

4.3. Solitary wave propagation in a variable water depth

This example is to validate the model ability of predicting the transformation of solitary wave propagation over a variable water depth. It has been found theoretically and experimentally that an initial solitary wave, propagating from one constant depth to another smaller constant depth, will disintegrate into several solutions of varying sizes, trailed by an oscillatory tail. This is called fission phenomenon [30, 32].

In this test, a solitary wave propagating from a constant depth $h_0 = 7.62$ cm, past a 1:20 slope, on to a smaller constant depth $h_1 = 3.81$ cm is simulated. An initial amplitude
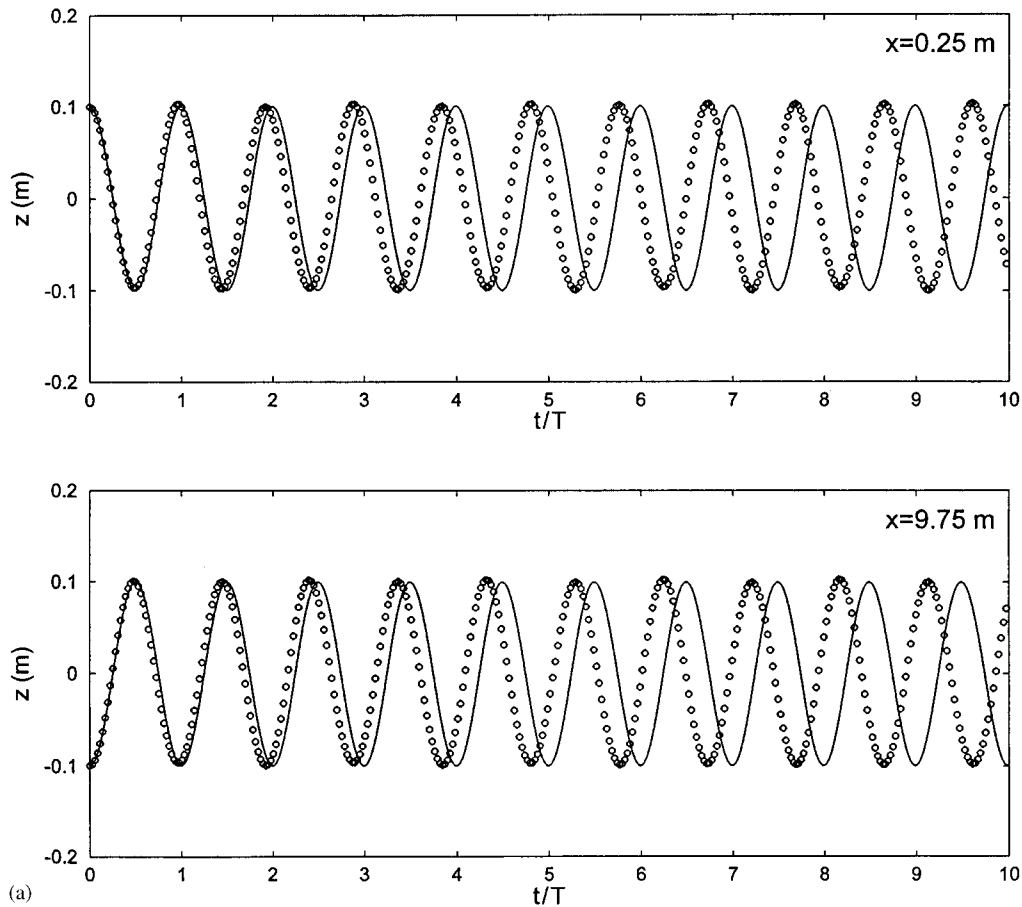
Figure 4. Comparisons of free-surface elevation for standing wave oscillation in a closed basin between numerical results (circles) and analytical solutions (solid lines) at $x = 0.25$ and 9.75 m using (a) non-hydrostatic model with hydrostatic pressure representation at the top layer, and (b) fully non-hydrostatic model.
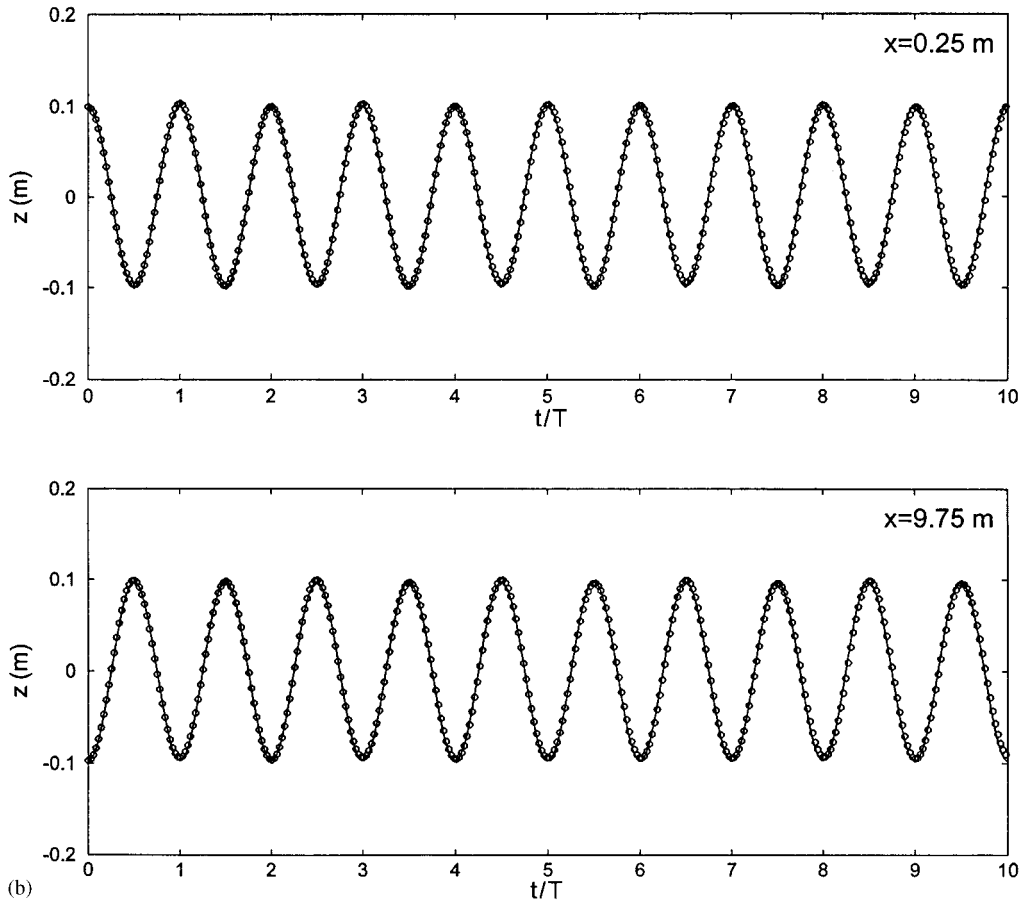
(b)

Figure 4. *Continued.*

to the water depth ratio, $A_0/h_0 = 0.12$, is set, and the sketch of bottom profile is shown in Figure 8. The initial wave celerity is $c = \sqrt{g(h_0 + A_0)} = 0.915\,\text{m/s}$. The computational domain with the length of 6 m is discretized by a set of uniform $M \times N = 600 \times 10$ cells. A time step of $\Delta t = 0.01$ s is chosen. Similarly to the last example, free-surface elevation and velocities based upon the analytical solution [31] at left inflow boundary are specified. The radiation boundary condition is imposed at the outflow boundary. Nevertheless the initial position of wave crest is specified at $x = -0.8$ m.

In Figure 9, the numerical results for the free-surface elevation at four locations are compared to the theoretical predictions and experimental data from Madsen and Mei [33]. The fission phenomenon is well observed in the numerical results. For comparison, the analytical predictions and experimental data are obtained by digitizing the figures in Reference [33]. The beginning time $t = 0$ s in Figure 8 corresponds to the computational time $t^* = 2.62$ s when the wave crest arrives the position 1. The numerical results of the maximum wave amplitude at positions 3 and 4 are in good agreement with estimated experimental amplitude for no viscous
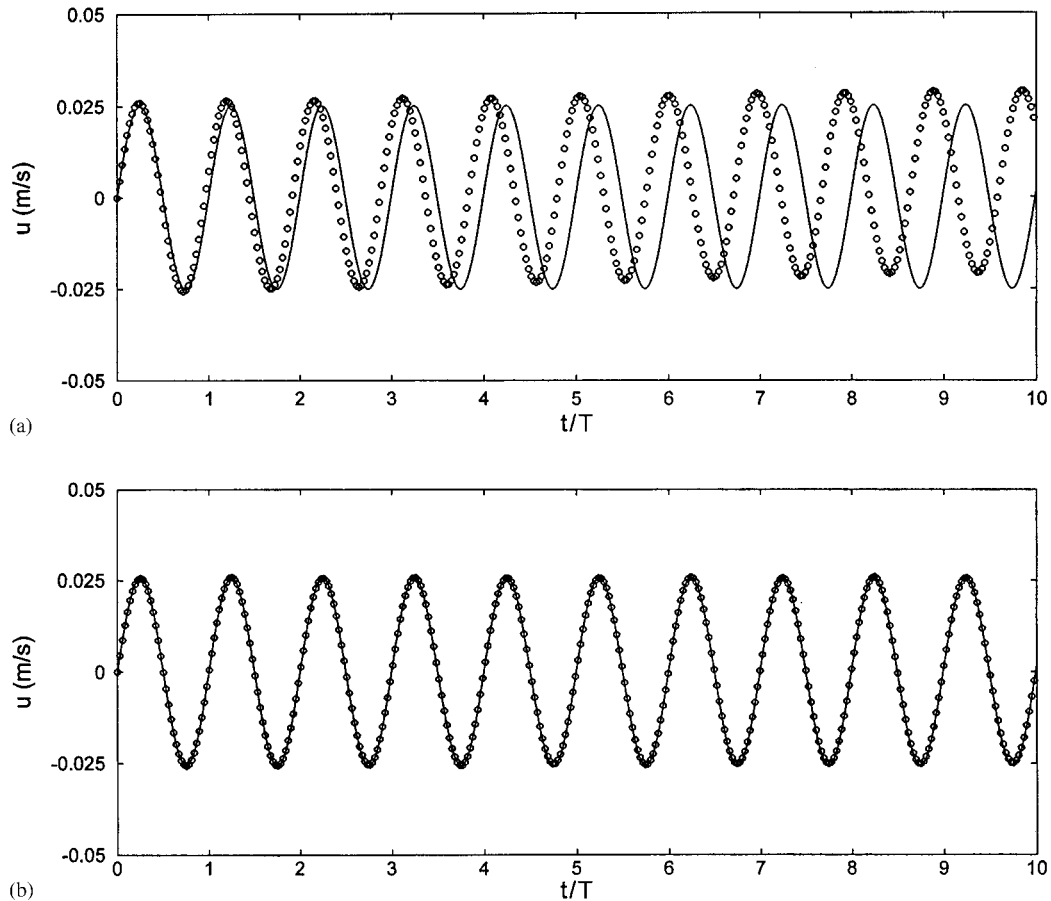
Figure 5. Comparisons of horizontal velocity at the middle elevation of the water depth at $x = 2.25$ m for standing wave oscillation in a closed basin between analytical solutions (solid lines) and numerical results (circles) from different models: (a) non-hydrostatic model with hydrostatic pressure representation at the top layer, and (b) fully non-hydrostatic model.

damping [33]. At position 4, the present model predicted the relative height of 145% for the larger wave and 68% for the smaller wave, compared to the initial wave height. This result is quantitatively consistent with other numerical and analytical approximations (e.g. 150 and 52% from Reference [32], 167 and 71% for a longer distance analytical approximation from Reference [33]). The success of the test indicates the potential of the present model to predict the transformation of solitary wave propagation over variable water depth.

4.4. Periodic wave propagation over a submerged bar

The final example is to periodic wave propagation over a submerged bar. The objective is to test the capability of the present model to simulate the relative strong interaction between non-linear wave and uneven bottom. This problem has been experimentally and numerically

Table I. Comparisons of numerical errors of the free-surface elevation under different Courant number Cr for standing wave oscillation in a closed basin.

Δt(s)	Cr	$L_{CYC}/2A$ over $1T$		$L_{CYC}/2A$ over $10T$	
		$x = 0.25$ m (%)	$x = 9.75$ m (%)	$x = 0.25$ m (%)	$x = 9.75$ m (%)
0.0001	0.001	0.9	0.7	1.0	0.9
0.001	0.012	0.9	0.7	2.0	1.9
0.01	0.115	0.8	0.9	1.8	1.7
0.05	0.558	0.9	1.0	1.8	1.8
0.1	1.115	3.4	4.0	4.1	4.0
0.2	2.230	7.5	8.1	10.9	10.7

Table II. Mesh convergence test in terms of the free-surface elevation using different mesh resolutions for standing wave oscillation in a closed basin.

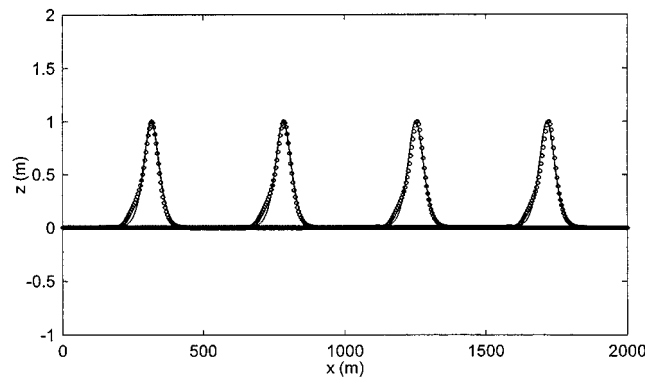| Mesh resolution (x-resolution $\times$ σ-resolution)	Cr	$L_{CYC}/2A$ over $1T$		$L_{CYC}/2A$ over $10T$	
		$x = 0.25$ m (%)	$x = 9.75$ m (%)	$x = 0.25$ m (%)	$x = 9.75$ m (%)
10×10		4.9	5.0	30.1	33.7
20×10		4.8	4.6	25.1	21.3
	0.558				
20×20		0.9	1.0	1.8	1.8
40×20		0.8	0.9	1.4	1.4

Figure 6. Comparisons of the free-surface elevation for solitary wave propagation in a constant water depth between numerical results (circles) and analytical solutions (solid line) at $t = 45, 90, 135$ and 180 s (from left to right).

investigated by numerous authors [14, 16–18, 20, 34–37]. It has been found that the shoaling would occur on the upward slope and the non-linearity would generate significant higher harmonics, which travel phase-locked to the primary wave. Model results based on the hydrostatic pressure assumption, neglecting the dispersion terms (corresponding to the non-hydrostatic pressure), are totally different and unrealistic [18].
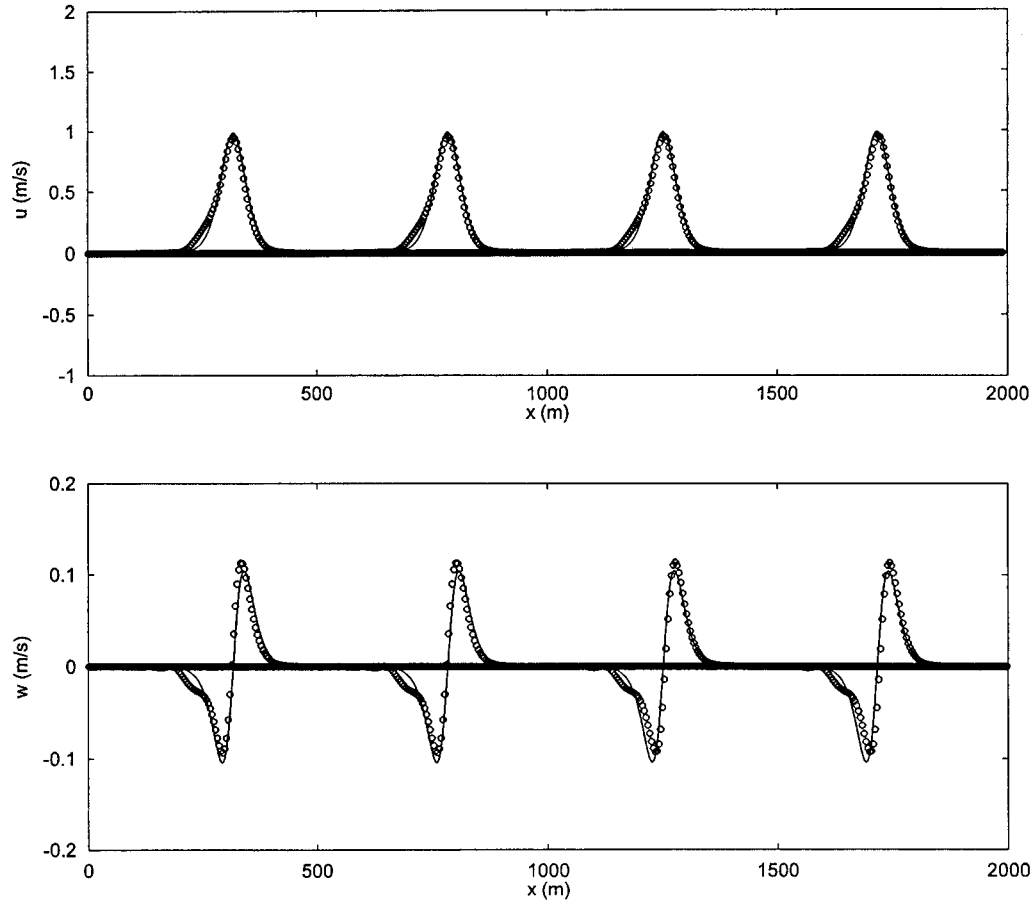
Figure 7. Comparisons of u and w at the middle elevation of the water depth for solitary wave propagation in a constant water depth between numerical results (circles) and analytical solutions (solid line) at $t = 45, 90, 135$ and 180 s (from left to right).

In this test, the experiments set-up carried by Beji and Battijes [35] is used for the numerical simulation. The geometry for the numerical computation is depicted in Figure 10. The water depth is $h_0 = 0.4$ m. At the inflow boundary a progressive wave with a wave height of $H_0 = 2.0$ cm and a period of $T_0 = 2.0$ s is specified. At the outflow boundary, difficulties of representing the absorbing beach with a 1:25 slope in the physical experiment set-up have been addressed by many authors. Zhou and Stansby [14] employed a reconstructed artificial beach portion near the shallow water region in their numerical the sigma model to avoid the difficulty in dealing with wetting/drying conditions. An open boundary condition like a radiation boundary condition (RBC) is usually used to represent experimental wave absorbers in other sigma models [13, 20] and the Boussinesq-type model [35]. In addition, the sponge layer technique coupled with the radiation boundary is also used to serve as numerical wave absorber [36, 37]. In this study, both the RBC and the sponge layer technique coupled with RBC are used to replace the original beach. We find that there is no noticeable difference
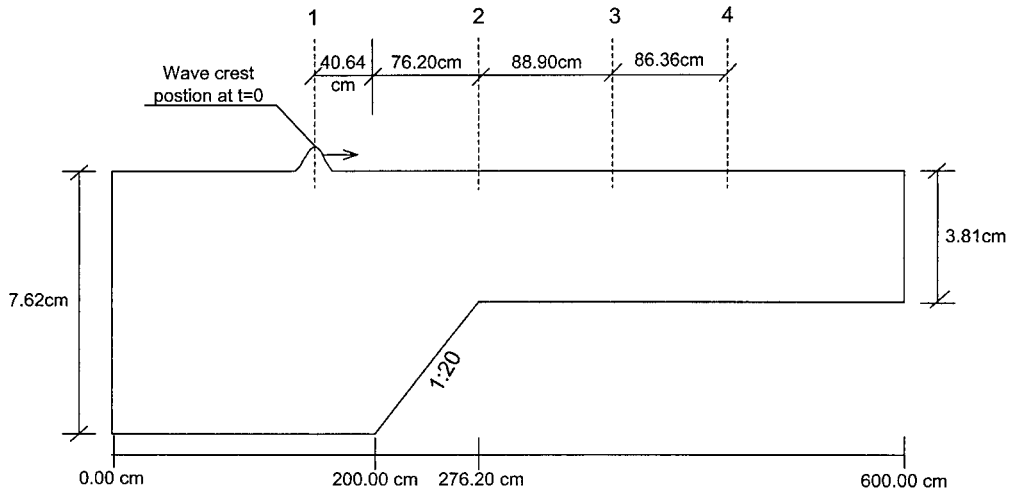
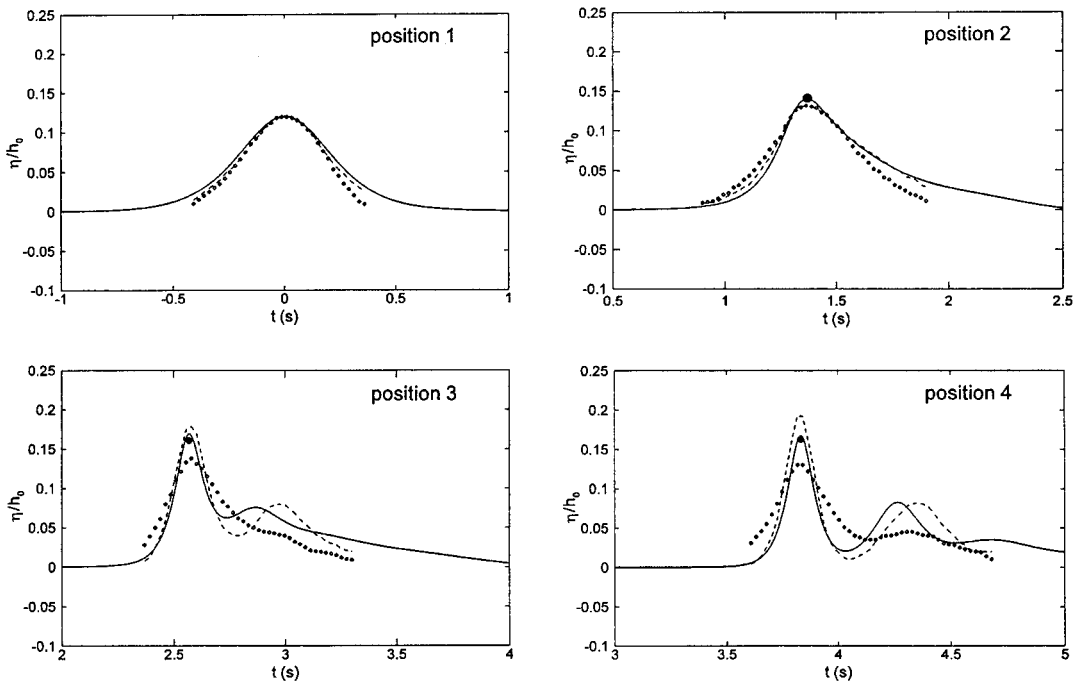Figure 8. Sketch of the geometry for solitary wave propagation in a variable water depth.

Figure 9. Comparisons of the free-surface elevation for solitary wave propagation in a variable water depth at location 1, 2, 3 and 4 among numerical results (solid line), theoretical predictions (dashed line) and experimental data (circles). Dots represent the estimated experimental amplitude for no viscous damping.
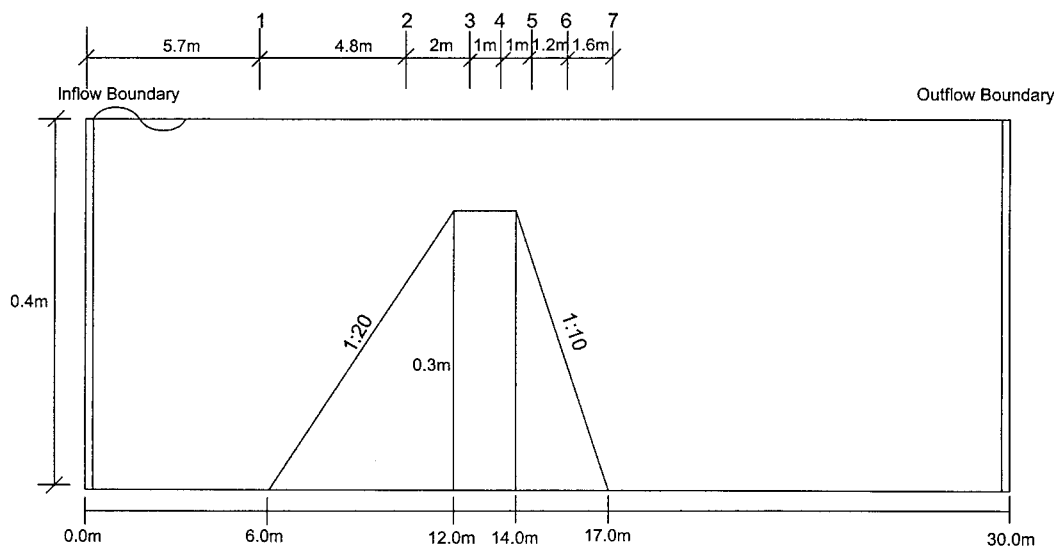
Figure 10. Sketch of the geometry for periodic wave propagation over a submerged bar.

in the simulation results between these two treatments. Therefore, only the numerical results using the RBC are shown in here.

The computational domain is discretized by a set of uniform $M \times N = 600 \times 20$ cells, and a time step of $\Delta t = 0.02$ s is chosen. The comparisons between the numerical results from the present model and experimental data from [35], for the free-surface elevation at four different wave gauge locations, are shown in Figure 11. At position 1, the wave remains sinusoidal and the numerical results are in excellent agreement with experimental data. From $x = 6$ to 12 m, the wave steepness is increased due to shoaling effects. At position 2, the model predicted a value of 1.2 for shoaling coefficient (equivalent to the relative wave height η/H_0), which agrees well with 1.182 from the analytical solution [29] and the experimental data. The model also well simulates the wave riding over the bar at position 3 and the secondary wave mode at position 5. The overall agreements between the numerical results and experiments indicate that the present model is capable to simulate the interaction between non-linear short wave and uneven bottom.

5. CONCLUSIONS

An implicit σ model for non-hydrostatic, free-surface flows in two-dimensional vertical plane has been developed. The vertical momentum equation is fully considered without the hydro-static assumption. In addition, a consistent non-hydrostatic-type pressure boundary condition at the top-layer cells, in contrast to the hydrostatic approximation in previous studies, is developed and found to be important for resolving the phase of wave propagation. The employment of the σ co-ordinate ensures an accurate representation of the flow at the bed and the free surface. Using the implicit method, all the flow field components are solved together within
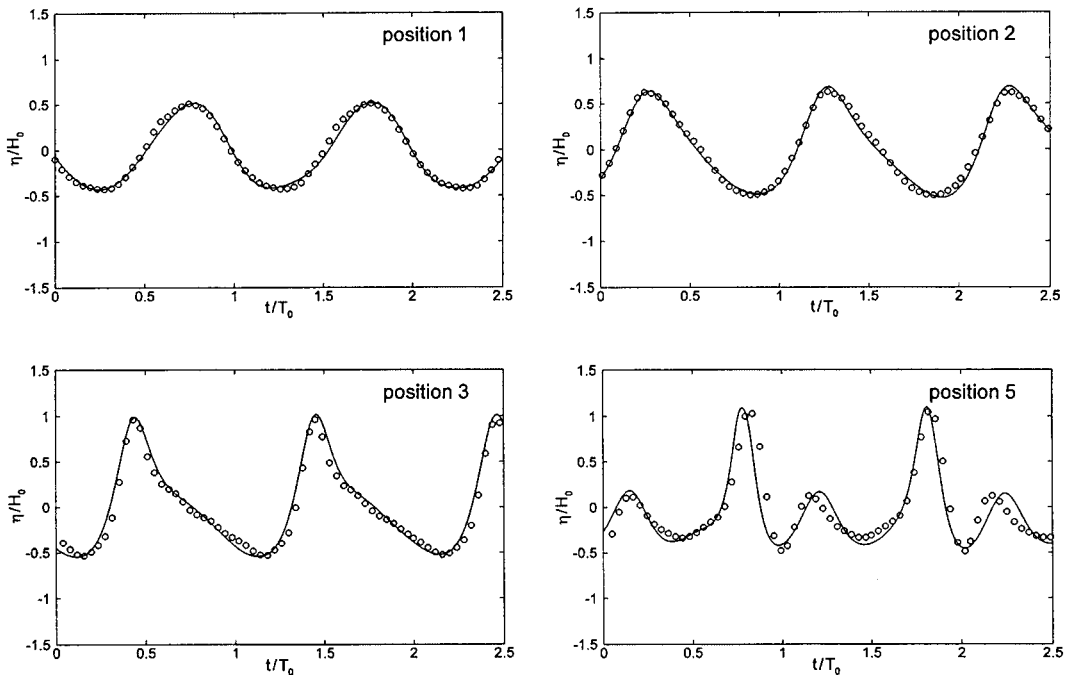
Figure 11. Comparisons of the free-surface elevation between numerical results (solid lines) and experimental data (circles) at four wave gauge locations: $1, 2, 3$ and 5.

one time step, and the resulting block tri-diagonal matrix system can be directly solved. The model has the advantage of simulating free-surface flows with less restricted time steps, in comparison to those based on the explicit numerical schemes.

The developed model is validated by a series of free-surface flow examples with significant vertical accelerations. For the case of standing wave oscillation in a closed basin, the model predicts very accurate results for the free-surface elevation, velocities and dynamic pressure. In modelling solitary wave propagation in a constant water depth, the numerical results for free-surface elevation and velocities are also in excellent agreement with analytical solutions. Numerical predictions for solitary wave propagation in a variable water depth and periodic wave propagation over a bar are also tested. The agreement between numerical results and experimental data is generally good, indicating that the model is capable of simulating interactions of non-linear waves and bottoms with complicated geometry.

Numerical tests show that results for simulating short waves and long waves are not sensitive to the implicit weighting factors (refer to Section 4) in the model. By setting a constant value of the implicit parameter (0.9 is used in this study), the present σ model can predict relative good results for a range of applications without further adjusting the factors. The validated model is being extended to three dimensions, taking into account the numerical errors introduced by the σ co-ordinate transformation for flows over steep topography. The basic idea is to decompose a three-dimensional problem into a series of two-dimensional systems associated with each corresponding vertical plane. A block tri-diagonal solver can then be used for solving each two-dimensional system. Comparison between the three-dimensional

block tri-diagonal system and PPE system in terms of relative computational efficiency will be given in the future.

REFERENCES

 1. Blumberg AF, Mellor GL. A description of a three-dimensional coastal ocean circulation model. In *Three-Dimensional Coastal Ocean Circulation Models*, *Coastal and Estuarine Sciences*, Heaps NS (ed.), vol. 4. AGU: Washington, DC, 1987; 1–16.
 2. Cheng RT, Casulli V, Gartner JW. Tidal, residual, intertidal mudflat (TRIM) model and its applications to San Francisco Bay, California. *Estuarine Coastal and Shelf Science* 1993; **36**:235–280.
 3. Sheng YP. On modeling three-dimensional estuarine and marine hydrodynamics. In *Three-Dimensional Models of Marine and Estuarine Dynamics*, Nihoul J, Jamart B (eds). Elsevier: Amsterdam, Netherlands, 1987; 35–54.
 4. Martin JL, McCutcheon SC. *Hydrodynamics and Transport for Water Quality Modeling*. CRC Press Inc.: New York, 1999.
 5. Mahadevan A, Oliger J, Street R. A non-hydrostatic mesoscale ocean model. Part 1: Well posedness and scaling. *Journal of Physical Oceanography* 1996; **26**(9):1868–1880.
 6. Marshall J, Hill C, Perelman L, Adcroft A. Hydrostatic, quasi-hydrostatic, and nonhydrostatic ocean modeling. *Journal of Geophysical Research* 1997; **102**(C3):5733–5752.
 7. Liu PLF, Losada IJ. Wave propagation modeling in coastal engineering. *Journal of Hydraulic Research* 2002; **40**(3):229–240.
 8. Tsai WT, Yue DKP. Computation of nonlinear free-surface flows. *Annual Review of Fluid Mechanics* 1996; **28**:249–278.
 9. Harlow FH, Welch JE. Numerical calculation of time-dependent viscous incompressible flow. *Physics of Fluids* 1965; **8**:2182–2189.
10. Hirt CW, Nichols BD. Volume of fluid (VOF) method for the dynamic of free boundaries. *Journal of Computational Physics* 1981; **39**:201–255.
11. Chan RKC. A generalized arbitrary Lagrangian–Eulerian method for incompressible flows with sharp interface. *Journal of Computational Physics* 1975; **17**:311–331.
12. Park JC, Kim MH, Miyata H. Fully non-linear free-surface simulations by a 3D viscous numerical wave tank. *International Journal for Numerical Methods in Fluids* 1999; **29**(6):685–703.
13. Lin P, Liu PLF. A numerical study of breaking waves in surf zone. *Journal of Fluid Mechanics* 1998; **359**: 239–264.
14. Zhou JG, Stansby PK. An arbitrary Lagrangian–Eulerian (ALES) model with non-hydrostatic pressure for shallow water flows. *Computer Methods in Applied Mechanics and Engineering* 1999; **178**:199–214.
15. Mayer S, Garapon A, Sorensen LS. A fractional step method for unsteady free-surface flow with applications to non-linear wave dynamics, *International Journal for Numerical Methods in Fluids* 1998; **28**(2):293–315.
16. Lin P, Li CW. A σ-coordinate three-dimensional numerical model for surface wave propagation. *International Journal for Numerical Methods in Fluids* 2002; **38**:1045–1068.
17. Casulli V, Zanolli P. Semi-implicit numerical modeling of nonhydrostatic free-surface flows for environmental problems. *Mathematical and Computer Modeling* 2002; **36**:(9–10):1131–1149.
18. Casulli V. A semi-implicit finite difference method for non-hydrostatic, free-surface flows. *International Journal for Numerical Methods in Fluids* 1999; **30**:425–440.
19. Chorin AJ. Numerical solution of the Navier–Stokes equations. *Mathematics of Computation* 1968; **22**: 745–762.
20. Li B, Fleming C. Three-dimensional model of Navier–Stokes equations for water waves. *ASCE Journal of Waterway, Port, Coastal, and Ocean Engineering* 2001; **127**(1):16–25.
21. Namin M, Lin B, Falconer R. An implicit numerical algorithm for solving non-hydrostatic free-surface flow problems. *International Journal for Numerical Methods in Fluids* 2001; **35**:341–356.
22. Kocyigit M, Falconer R, Lin B. Three-dimensional numerical modeling of free surface flows with non-hydrostatic pressure. *International Journal for Numerical Methods in Fluids* 2002; **40**:1145–1162.
23. Kowalik Z, Murty TS. *Numerical Modeling of Ocean Dynamics*. World Scientific: Singapore, 1993.

24. Phillips NA. A coordinate system having some special advantages for numerical forecasting. *Journal of Meteorology* 1957; **14**:184–185.
25. Haney RL. On the pressure gradient force over steep topography in σ coordinate ocean models. *Journal of Physical Oceanography* 1991; **21**:610–619.
26. Stelling G, van Kester JATM. On the approximation of horizontal gradients in sigma co-ordinates for bathymetry with steep bottom slopes. *International Journal for Numerical Methods in Fluids* 1994; **18**:915–935.
27. Song YT. A general pressure gradient formulation for ocean models, Part I: Scheme design and diagnostic analysis. *Monthly Weather Review* 1998; **126**:3212–3230.
28. Tannehill JC, Anderson DA, Pletcher RH. Computational fluid mechanics and heat transfer. In *Series in Computational and Physical Processes in Mechanics and Thermal Sciences*, Minkowycz WJ, Sparrow EM (eds), (2nd edn). Taylor & Francis; Hemisphere Publishing Corporation: Bristol, PA, 1997; 717–724.
29. Dean RG, Dalrymple RA. *Water Wave Mechanics for Engineers and Scientists*. World Scientific: Singapore, 2000.
30. Mei CC. *The Applied Dynamics of Ocean Surface Waves*. Wiley Inter-science: New York, 1983.
31. Lee J-J, Skjelbreia E, Raichlen F. Measurement of velocities in solitary waves. *Journal of Waterway*, *Port*, *Coastal and Ocean Division* 1982; **108**(WW2):200–218.
32. Woo SB, Liu PLF. A Petrov–Galerkin finite element model for one-dimensional fully non-linear and weakly dispersive wave propagation. *International Journal for Numerical Methods in Fluids* 2001; **37**:541–575.
33. Madsen OS, Mei CC. The transformation of a solitary wave over an uneven bottom. *Journal of Fluid Mechanics* 1969; **39**(4):781–791.
34. Beji S, Battjes JA. Experimental investigation of wave propagation over a bar. *Coastal Engineering* 1993; **19**:151–162.
35. Beji S, Battjes JA. Numerical simulation of non-linear waves propagation over a bar. *Coastal Engineering* 1994; **23**:1–16.
36. Beji S, Ohyama T, Battjes JA, Nadaoka K. Transformation of nonbreaking waves over a bar. In *Coastal Engineering Proceedings of the 23rd International Conference*, vol. 1, Venice, Italy, 1992; 51–61.
37. Stelling G, Zijlema M. An accurate and efficient finite-difference algorithm for non-hydrostatic free-surface flow with application to wave propagation. *International Journal for Numerical Methods in Fluids* 2003; **43**:1–23.